

Observed Relationships between Cloud Vertical Structure and Convective Aggregation over Tropical Ocean

T. H. M. STEIN AND C. E. HOLLOWAY

Department of Meteorology, University of Reading, Reading, United Kingdom

I. TOBIN

LSCE/IPSL/CNRS, Gif sur Yvette, France

S. BONY

LMD/IPSL, CNRS, UPMC, Paris, France

(Manuscript received 9 February 2016, in final form 8 December 2016)


ABSTRACT

Using the satellite-infrared-based Simple Convective Aggregation Index (SCAI) to determine the degree of aggregation, 5 years of *CloudSat*–*CALIPSO* cloud profiles are composited at a spatial scale of 10 degrees to study the relationship between cloud vertical structure and aggregation. For a given large-scale vertical motion and domain-averaged precipitation rate, there is a large decrease in anvil cloud (and in cloudiness as a whole) and an increase in clear sky and low cloud as aggregation increases. The changes in thick anvil cloud are proportional to the changes in total areal cover of brightness temperatures below 240 K [cold cloud area (CCA)], which is negatively correlated with SCAI. Optically thin anvil cover decreases significantly when aggregation increases, even for a fixed CCA, supporting previous findings of a higher precipitation efficiency for aggregated convection. Cirrus, congestus, and midlevel clouds do not display a consistent relationship with the degree of aggregation. Lidar-observed low-level cloud cover (where the lidar is not attenuated) is presented herein as the best estimate of the true low-level cloud cover, and it is shown that it increases as aggregation increases. Qualitatively, the relationships between cloud distribution and SCAI do not change with sea surface temperature, while cirrus clouds are more abundant and low-level clouds less at higher sea surface temperatures. For the observed regimes, the vertical cloud profile varies more evidently with SCAI than with mean precipitation rate. These results confirm that convective scenes with similar vertical motion and rainfall can be associated with vastly different cloudiness (both high and low cloud) and humidity depending on the degree of convective aggregation.

1. Introduction

Mean rainfall and convective activity are intrinsically linked (e.g., [Arkin and Meisner 1987](#)). Increases in tropical rainfall in recent years have been associated with a shift toward more frequent organized convection ([Tan et al. 2015](#)). Although such a response is consistent with a warming climate (e.g., [Trenberth et al. 2003](#)), observations and GCMs do not agree on the rate at which precipitation

increases with surface temperature ([Allan and Soden 2008](#); [Pendergrass and Hartmann 2014](#)). Elucidating the role of convective aggregation in crucial aspects of weather and climate, including extreme events, tropical intraseasonal oscillations, and hydrological and climate sensitivities, was recently recognized as one of the “grand challenges” for climate science ([Bony et al. 2015](#)). Numerical studies constitute a powerful way to address this issue. However, given uncertainties in the numerical prediction of clouds, investigations of the link between convective aggregation and clouds should include observations.

 Denotes content that is immediately available upon publication as open access.

Corresponding author e-mail: T. H. M. Stein, t.h.m.stein@reading.ac.uk



This article is licensed under a [Creative Commons Attribution 4.0 license](http://creativecommons.org/licenses/by/4.0/). (<http://creativecommons.org/licenses/by/4.0/>).

DOI: 10.1175/JCLI-D-16-0125.1

© 2017 American Meteorological Society.

Simulations of idealized radiative–convective equilibrium (RCE) have documented different equilibrium states for the same large-scale forcing (e.g., [Tompkins and Craig 1998](#); [Bretherton et al. 2005](#); [Stephens et al. 2008](#); [Muller and Held 2012](#); [Wing and Emanuel 2014](#)), not only with cloud-resolving models, but also with general circulation models (GCMs) ([Reed et al. 2015](#); [Coppin and Bony 2015](#)). In some conditions, convection undergoes “self-aggregation,” becoming clustered in small regions that have high column-integrated water vapor and precipitation while the rest of the domain becomes much drier. In other conditions, convection stays mainly disaggregated, with scattered convection and higher domain-mean humidity. Some studies, particularly [Muller and Held \(2012\)](#), have also shown some dependence on horizontal resolution, domain size, and initial conditions. Cold pools may inhibit aggregation ([Jeevanjee and Romps 2013](#)), and suppression of cold pools can allow self-aggregation even when radiative heating rates are fixed ([Muller and Bony 2015](#); [Holloway and Woolnough 2016](#)).

Several studies have shown a threshold behavior of self-aggregation with respect to sea surface temperature (SST), with self-aggregation not occurring below an SST threshold; [Khairoutdinov and Emanuel \(2010\)](#) found such a threshold near 297 K, [Wing and Emanuel \(2014\)](#) found a threshold near 300 K (and another near 307 K, above which they did not see self-aggregation unless they increased their domain size), and [Emanuel et al. \(2014\)](#) found a critical SST threshold between 303 and 308 K. These values are near the current most common observed SST in tropical convective regions, as well as the maximum observed SST. [Khairoutdinov and Emanuel \(2010\)](#) hypothesized that tropical SST may exhibit self-organized criticality, with feedbacks between aggregation state and net surface fluxes that tend to cool SSTs in aggregated conditions (above the SST threshold) and warm SSTs in disaggregated conditions, thus maintaining SSTs near the threshold in convective regions. This hypothesis has been questioned by observational studies (see below) and recent modeling studies ([Wing and Cronin 2016](#); [Holloway and Woolnough 2016](#)). Nevertheless, understanding the mechanisms and role of self-aggregation may be important for predicting weather phenomena such as tropical cyclone formation ([Davis 2015](#); [Wing et al. 2016](#)) and the Madden–Julian oscillation ([Arnold and Randall 2015](#)), and for climate prediction ([Mauritsen and Stevens 2015](#); [Bony et al. 2016](#)).

To determine relationships between convective aggregation and the large-scale atmosphere, [Tobin et al. \(2012\)](#) analyzed $10^\circ \times 10^\circ$ regions over warm tropical ocean using satellite observations. For a given SST and large-scale forcing, they found a dependence of domain-mean humidity and outgoing longwave radiation (OLR) on the

degree of aggregation that resembled the relationships found for these quantities in the aforementioned studies of RCE in models. [Tobin et al. \(2013\)](#) performed similar analyses on somewhat smaller scales and found similar relationships, although the two studies have somewhat different findings regarding the net surface flux tendencies in aggregated versus disaggregated states, suggesting that the self-organized criticality mechanism hypothesized in [Khairoutdinov and Emanuel \(2010\)](#) may not be supported by observations. [Tobin et al. \(2013\)](#) also analyzed International Satellite Cloud Climatology Project (ISCCP) data and found larger amounts of clear sky and low-level cloud, and smaller amounts of midlevel cloud and cirrostratus, with increased aggregation.

The results from [Tobin et al. \(2012\)](#) suggest that, for a given precipitation rate, aggregated convection will have a higher precipitation efficiency than disaggregated convection. Many questions remain, however, about how clouds outside of deep convective storms respond to large-scale forcing and to the degree of convective aggregation, such as the following:

- Low-level clouds dominate in large parts of the tropical ocean and have a cooling effect on Earth’s surface, but does the low cloud amount decrease or increase as convective aggregation increases and the anvil cloud amount decreases?
- Cumulus congestus are often not considered in studies of tropical rainfall, despite their frequency and considerable contribution to total rainfall ([Johnson et al. 1999](#); [Liu and Zipser 2009](#)); do such clouds persist when deep convection is aggregated?
- Anvil clouds are a direct result of deep convection detraining near the tropopause, but are the anvil characteristics such as height, thickness, and relative frequency per deep convective cloud related to the degree of aggregation?

To address such questions, we have analyzed individual cloud layers identified over nearly 5 years of data (July 2006–April 2011) from two A-Train satellites, *CloudSat* and the *Cloud-Aerosol Lidar and Infrared Pathfinder Satellite Observations (CALIPSO)* ([Stephens et al. 2002](#)). The cloud profiling radar aboard *CloudSat* and the *CALIPSO* lidar observe the same cloud scenes, and the strengths of the two instruments are combined to provide near-complete cloud profiles, from thin cirrus through deep convection down to shallow cumulus. Analysis of cloud-type occurrence has highlighted the prominence of congestus and midlevel detrainment in the West African monsoon ([Stein et al. 2011b](#)), and the identification of individual convective cloud features in *CloudSat* data has related deep convective characteristics to SSTs ([Igel et al. 2014](#)).

In this paper, we seek to explore the dependence of vertical cloud structure and cloud type on convective aggregation in greater detail using *CloudSat*–*CALIPSO* data. We summarize the methodology from Tobin et al. (2012) and the design of the Simple Convective Aggregation Index (SCAI) in section 2. The compositing techniques and cloud-type classification from *CloudSat*–*CALIPSO* data are described in section 3. In section 4, we show our results for the vertical distribution of cloud fraction. Fractional cover from different cloud types is presented in section 5, where we also consider the effect of optically thin clouds on clear-sky identification; low-level clouds are discussed separately in section 6. The sensitivity of our analysis to different SST values is discussed in section 7 and a summary of key findings and their implications and potential future work are provided in section 8.

2. The Simple Convective Aggregation Index

Tobin et al. (2012) define the Simple Convective Aggregation Index as follows:

$$\text{SCAI} = \frac{N}{N_{\max}} \frac{D_0}{L} \times 1000, \quad (1)$$

where N is the number of clusters, N_{\max} is the maximum possible number of clusters in the domain (which is half the total number of pixels), L is the length scale of the domain, and D_0 is the geometric mean distance between the centroids of all clusters. Clusters are composed of cold-cloud pixels using 4-connectivity, with cold-cloud pixels identified below a brightness temperature of 240 K. Brightness temperatures are at 4-km resolution from window-channel ($\approx 10.7\mu\text{m}$) infrared data merged by the Climate Prediction Center from several geostationary satellites (Janowiak et al. 2001). Arithmetically speaking, SCAI increases both with number of clusters N and with mean distance D_0 (D_0 is set to 0 when there is only one cluster in the domain). Because of the dependence of D_0 on the spatial distances between the clusters, an increase in N could lead to both an increase and a decrease in D_0 , so that on a case-by-case basis SCAI may not necessarily increase as N increases. However, such marginal changes are not of interest in this study; broadly speaking, we will consider low SCAI values to describe aggregated convection and high SCAI values disaggregated convection. Similar to Tobin et al. (2012), our analysis does not lead to different conclusions when we consider number of clusters N instead of SCAI.

In our analysis, mean rainfall rates are calculated from the Tropical Rainfall Measurement Mission (TRMM)

3B42 product (Huffman et al. 2007), which incorporates the same brightness temperature data as our SCAI calculations. SCAI values and mean rainfall rates are calculated for every 3 h in time (0000, 0300, 0600 UTC, etc.) and for $10^\circ \times 10^\circ$ grid boxes between 30°S and 30°N , with boxes overlapping 5° in both latitude and longitude. As a result of the high resolution of brightness temperature data, N_{\max} is larger and SCAI values are lower compared to those reported by Tobin et al. (2012); in particular, the 80th and 95th percentiles of SCAI are 0.61 and 1.36 using our method and data compared with 13 and 19, respectively, for their study. SCAI values are considered between 0 and 1.5 and precipitation rates, R , are considered between 4.5 and 10.5 mm day^{-1} with 1 mm day^{-1} bins.

In addition to SCAI and R , we also consider the cold cloud area (CCA) on the same grid, which is the fractional area of all pixels with brightness temperature below 240 K. To provide context for our study, column-integrated water vapor and CCA are plotted as functions of SCAI for several rainfall rates in Fig. 1. Column-integrated water vapor is obtained from ERA-Interim reanalysis (Dee et al. 2011), with the average calculated for each $10^\circ \times 10^\circ$ grid box; the 6-hourly instantaneous values from ERA-Interim were repeated for the next 3-hourly time to match the temporal resolution of the SCAI and R values. As found in Tobin et al. (2012) and Tobin et al. (2013), the domain mean is drier and the CCA (which they call convective area) is lower for lower SCAI (more aggregation) at a given rain rate.

Several restrictions were imposed on *CloudSat*–*CALIPSO* observations used in this analysis in order to discount large-scale influence on convective organization and cloud occurrences. First, *CloudSat* and *CALIPSO* often cut across only a corner of a grid box so that stretches may have different number of profiles, although a minimum of 60 (approximately 100 km) was enforced and the results presented in this paper are weighted by number of profiles per stretch. Note that the grid used for SCAI is made up of overlapping boxes, so that partial orbit stretches may be sampled up to four times. Second, only grid boxes in the Indian Ocean and Pacific Ocean were included (less than 5% land) and only when the mean sea surface temperature was between 300.5 and 301.5 K (approximately 28°C); further SST ranges are briefly discussed in section 7. Third, vertical pressure velocity (ω) from ERA-Interim was averaged over the $10^\circ \times 10^\circ$ grid boxes at the 300-, 500-, and 800-hPa levels; the 6-hourly instantaneous values from ERA-Interim were repeated for the next 3-hourly time to match the temporal resolution of the SCAI and R values. A given *CloudSat*–*CALIPSO* orbit stretch was only analyzed when all three ω values were within ± 1 standard deviation of their respective medians for the R

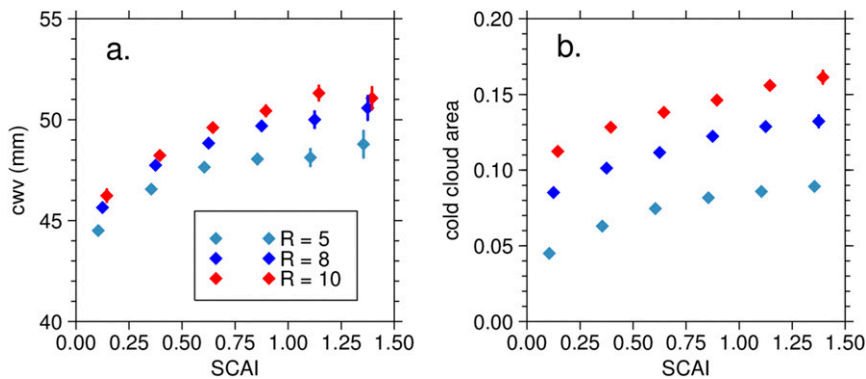


FIG. 1. (a) Domain-mean column-integrated water vapor (cww) in mm from ERA-Interim and (b) CCA vs SCAI, averaged for three rain rate bins (colors, in mm day^{-1}). Vertical lines show ± 1 standard error of the mean. Note that an artificial offset of ± 0.02 has been introduced in SCAI for high and low rain rates to aid in visual interpretation of the data.

bin associated with the orbit stretch. The second and third requirement, in combination with the restriction of precipitation regime R , will ensure as much as possible that the relationships analyzed in this paper are not driven by differing large-scale forcings. The total number of orbit stretches for each SCAI– R combination that meets these three requirements is listed in Table 1.

3. CloudSat–CALIPSO compositing analysis

CloudSat and CALIPSO are part of the A-Train constellation of satellites, which fly in a polar-orbiting configuration with equatorial overpasses around 0130 and 1330 LT with roughly 16 overpasses per day and a return period of about 16 days. The 94-GHz cloud-profiling radar aboard CloudSat observes ice aggregates and liquid precipitation, but is not sensitive to cloud ice dominated by small crystals such as in thin cirrus, or to liquid clouds composed of small droplets or low liquid water contents (e.g., Christensen et al. 2013b). Surface clutter contamination rules out the bottom 1 km of each CloudSat profile (Marchand et al. 2008). The CALIPSO lidar observes most cloud ice colder than -40°C (Stein et al. 2011a) but is easily attenuated by optically thick clouds before the signal can reach the surface. The lidar detects liquid clouds, allowing the identification of cumulus and stratus as well as supercooled liquid layers. The analysis presented here uses the radar–lidar (DARDAR) mask product (Delanoë et al. 2011), in which CloudSat and CALIPSO data are interpolated and averaged, respectively, on to a common grid with 60-m vertical resolution and 1.5 km horizontal footprint. All available orbits between June 2006 and April 2011 inclusive were used.

To composite cloud properties on SCAI and other convective indices, each CloudSat–CALIPSO orbit was

matched with the nearest 3-hourly time, t_i . For each $10^{\circ} \times 10^{\circ}$ grid box, the part of the satellite orbit that passed through it was included and stratified by the convective indices of that grid box at t_i . The further restrictions mentioned in the previous section also applied to the compositing analysis.

Using a selection of CloudSat quicklook images, we illustrate the different cloud type occurrences for four combinations of SCAI and R in Fig. 2. The images were randomly selected apart from a requirement of at least 800 profiles per image. It is clear from Fig. 2 that for low SCAI, clear skies and low-level cloud dominate the orbits, while deep clouds are concentrated. For high SCAI (Figs. 2c,d), deep clouds appear more numerous, though scattered across individual orbits; clear skies and low-level cloud are less prominent. For a given SCAI, there is no immediately apparent difference in cloud distributions between low rain rates and high rain rates when comparing Figs. 2a and 2b (or Figs. 2c and 2d), apart from a higher frequency of deep clouds.

TABLE 1. Total number of stretches of CloudSat–CALIPSO orbits considered for each combination of SCAI and rainfall rate (mm day^{-1}). Number of profiles per stretch may vary. SCAI and R ranges are indicated by their midpoints.

SCAI	Rainfall rate						All
	5	6	7	8	9	10	
0.125	612	378	260	170	138	89	1647
0.375	551	495	380	277	213	172	2088
0.625	307	252	241	191	163	157	1311
0.875	147	147	118	153	106	84	755
1.125	61	68	63	62	53	58	365
1.375	42	35	33	30	24	24	188
All	1720	1375	1095	883	697	584	6354

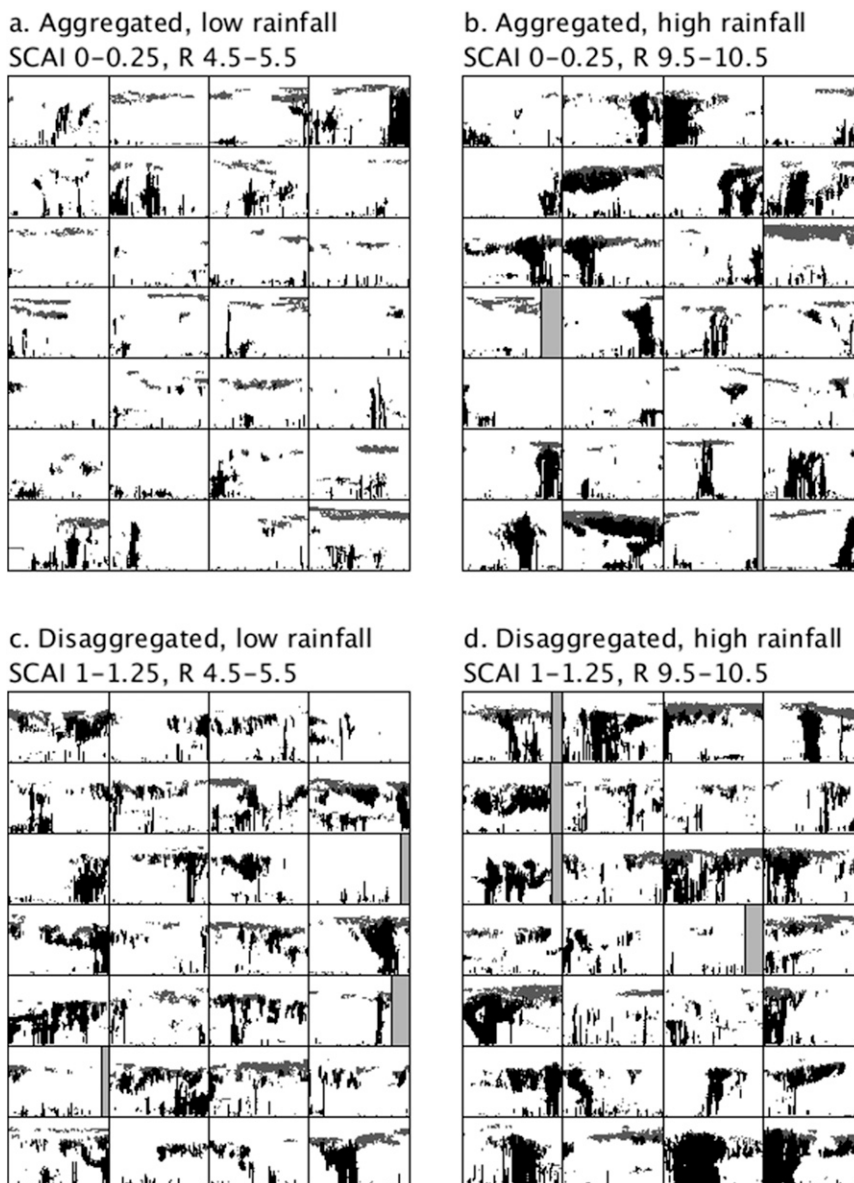


FIG. 2. Quicklook cloud mask images from up to 28 randomly selected orbits for four SCAI- R combinations. The *CloudSat* mask is shown in black, with *CALIPSO*-only cloud in dark gray. Individual images show 10° latitude by 20-km height, with light gray areas filling the box when a stretch is shorter than 10° .

We assume that the individual *CloudSat*-*CALIPSO* orbits are independent samples of the cloud-and-precipitation distribution for a given SCAI- R combination. Thus, the mean vertical cloud-and-precipitation structure will be obtained by combining all samples and, for each height, calculating the fraction of observations for which the *CloudSat* cloud mask or the *CALIPSO* mask detects cloud or precipitation. We will use the term “radar-lidar hydrometeor fraction” (RLH fraction) following Marchand et al. (2009) to indicate that no

distinction is made between cloud and precipitation in this analysis. Since some of the SCAI- R combinations have a low number of associated *CloudSat*-*CALIPSO* stretches, we use a bootstrapping method to calculate the mean RLH fraction. Thus, for a given population of M (number of) *CloudSat*-*CALIPSO* stretches, we resample this population drawing M stretches with replacement and derive the mean RLH fraction from this new set; we repeat this 1000 times to obtain 1000 estimates of the mean RLH fraction. This bootstrapping

method allows us to estimate a 90% confidence interval for the mean RLH fraction from the 1000 realizations and we choose the median of these 1000 means to denote the mean RLH fraction (van de Poll et al. 2006; Liu et al. 2010).

Finally, we will also comment on the Spearman rank correlation coefficient between RLH fraction or cloud-type cover and SCAI or CCA. The Spearman rank correlation does not assume a linear relationship between two variables, but it is a useful indication of a monotonic increase or decrease (statistical significance is set at $p < 0.05$). The purpose of the rank correlation is to avoid any assumptions on the behavior of an increase or decrease in cloud amounts with SCAI—beyond monotonicity—given that SCAI itself has a complex relationship involving both N and D_0 . Following Tobin et al. (2012), we performed our analysis of cloud distributions both using SCAI and using N and found qualitatively similar results. We therefore only consider SCAI in this study.

Cloud-type classification

The cloud classification presented here distinguishes cloud types by pressure levels, where pressure is provided in the DARDAR product through the ECMWF-AUX product. Cloud types are identified for each individual profile (i.e., no consistency across adjacent profiles is required). The delineation generally follows the method introduced by Stein et al. (2011b), as follows:

- 1) Low-level clouds have cloud top below the 700-hPa level (detection by radar and lidar is explored in section 6).
- 2) Midlevel clouds have cloud top between 350 and 700 hPa and base at least 1 km above the surface.
- 3) Congestus clouds have cloud top between 350 and 700 hPa and base within 1 km of the surface.
- 4) Nimbostratus and deep convective clouds have cloud top above the 350-hPa level and base within 1 km of the surface; deep convective clouds are further distinguished by having the maximum height of 10 dBZ above 8 km above mean sea level.
- 5) Anvil clouds have cloud top above the 350-hPa level and base at least 1 km above the surface (but no higher than the 200-hPa level); thin anvil clouds are further distinguished by having optical thickness less than 2.
- 6) Cirrus clouds have cloud base above the 200-hPa level.

Cloud types may be wrongly classified due to multiple scattering and attenuation (Battaglia et al. 2008), but these misclassifications affect only a small fraction of profiles and are not expected to depend on the compositing parameters SCAI and R .

The split between optically thick and optically thin anvil is introduced here as the latter usually do not contribute to CCA: down to 9 km, only 2.1% of profiles with cloud optical thickness (τ) between 1 and 2 have brightness temperatures less than 240 K; for optical thickness between 2 and 4 this increases to 22.1%. Optical thickness of cloud layers is determined by integrating the visible extinction coefficient, which is retrieved from *CloudSat*–*CALIPSO* observations using the Delanoë and Hogan (2010) optimal estimation algorithm and is available in the DARDAR cloud product. Of all the profiles with cirrus cloud layers, less than 2% had a cirrus cloud with optical thickness, τ , greater than 2, so no distinction between optically thick and optically thin cirrus was considered in the results. In addition to these cloud types, a profile in which no cloud layer is encountered is considered “clear sky.”

Low-level cloud detection becomes an issue because attenuation of the lidar signal by thick cloud aloft will lead to an underestimate of nondrizzling low-level clouds that have small liquid water contents. As explained above, optically thick anvil clouds are definitely correlated with CCA and may therefore be correlated with SCAI and R , so that potential reductions in low-level cloud cover with SCAI may simply be due to an increased occurrence of lidar attenuation. We expect that the *CloudSat* radar is less likely attenuated before it can detect low-level clouds, but its sensitivity to liquid clouds is much less than *CALIPSO*. Of all profiles with low-level cloud detected, 7% have detections by the *CloudSat* radar only, 67% by *CALIPSO* only, and 26% by both the *CloudSat* radar and *CALIPSO*. In section 6, we argue that fractional cover of low-level cloud detected by the lidar for profiles where the lidar is not attenuated is indicative of the true low-level cloud fraction regardless of SCAI and R .

4. Cloud vertical structure

In Figs. 3a–c, we show the mean radar–lidar hydrometeor fraction with height for height bins of 500 m, with means calculated for three ranges of precipitation rates and within each precipitation range for six ranges of SCAI values. For each precipitation range, between 3 and 14 km we see a clear increase of RLH fraction between SCAI values at 0–0.25 and those at 1.25–1.50, with the largest increase around 12 km. Between 6 and 14 km, the rank correlation between RLH fraction and SCAI is statistically significant with values of 0.63–1.00 across the R ranges (not shown), indicating that RLH fraction monotonically increases as SCAI increases at these heights. For heights between 16 and 18 km, the rank correlation indicates a monotonic decrease of RLH

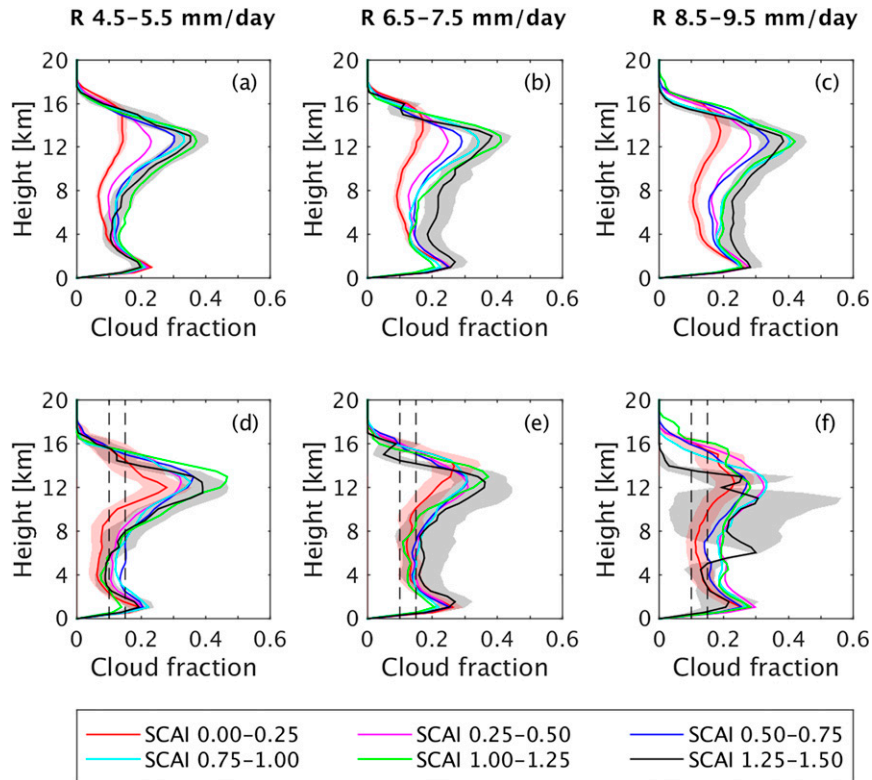


FIG. 3. Average radar–lidar hydrometeor (RLH) fraction for different ranges of SCAI, restricted to rainfall rates of (a) 4.5–5.5, (b) 6.5–7.5, and (c) 8.5–9.5 mm day⁻¹. Different colored lines indicate different SCAI ranges, namely 0–0.25 (red), 0.25–0.50 (magenta), 0.50–0.75 (blue), 0.75–1.00 (cyan), 1.00–1.25 (green), and 1.25–1.50 (black). Shaded areas depict the 90% confidence intervals for the lowest and highest SCAI ranges. (d)–(f) As in (a)–(c), but restricted to observations with CCA between 0.10 and 0.15 (indicated by the dashed vertical lines).

fraction as SCAI increases (not shown); this is discernible from Figs. 3a–c, as the RLH fraction for SCAI between 0 and 0.25 is greater than for SCAI between 1.25–1.50.

The increase of RLH fraction between 6 and 14 km may be partly due to the strong correlation between SCAI and cold cloud area. For example, more than 95% of *CloudSat*–*CALIPSO* profiles with brightness temperature below 240 K have cloud layers above 10 km, so we expect that the RLH fraction at such heights will show a positive correlation with CCA, which may be the underlying cause of the relationship with SCAI seen in Figs. 3a–c. Therefore, in Figs. 3d–f, we show the RLH fraction restricted to observations with CCA between 0.10 and 0.15. For all R ranges, several of the SCAI curves are now within the 90% confidence intervals of one another for much of the range between 3 and 15 km, although the extreme aggregation cases are still significantly different. The cloud fraction around 13 km is considerably higher than the range of CCA values

considered, which we attribute to optically thin clouds that do not contribute to CCA. The cumulative contribution to RLH fraction by brightness temperature (not shown) indicates that at 12 km only 30% of the total RLH fraction comes from profiles with brightness temperatures below 240 K; the remainder is from (optically thin) high clouds in profiles with warmer brightness temperatures. Therefore, for a given CCA, we should expect the high-level RLH fraction to be several times that value, regardless of the degree of aggregation between the convective clusters. This explains why the RLH fraction around 13 km is greater than the CCA in Figs. 3d–f.

In Fig. 4 we show the same analysis as in Fig. 3, but excluding *CALIPSO* observations in an attempt to exclude optically thin clouds. The decrease in RLH fraction as SCAI increases for height below 1 km and between 16 and 18 km is no longer evident in Figs. 4a–c, suggesting that the majority of the RLH fraction in Fig. 3 at these heights is due to clouds with relatively low liquid

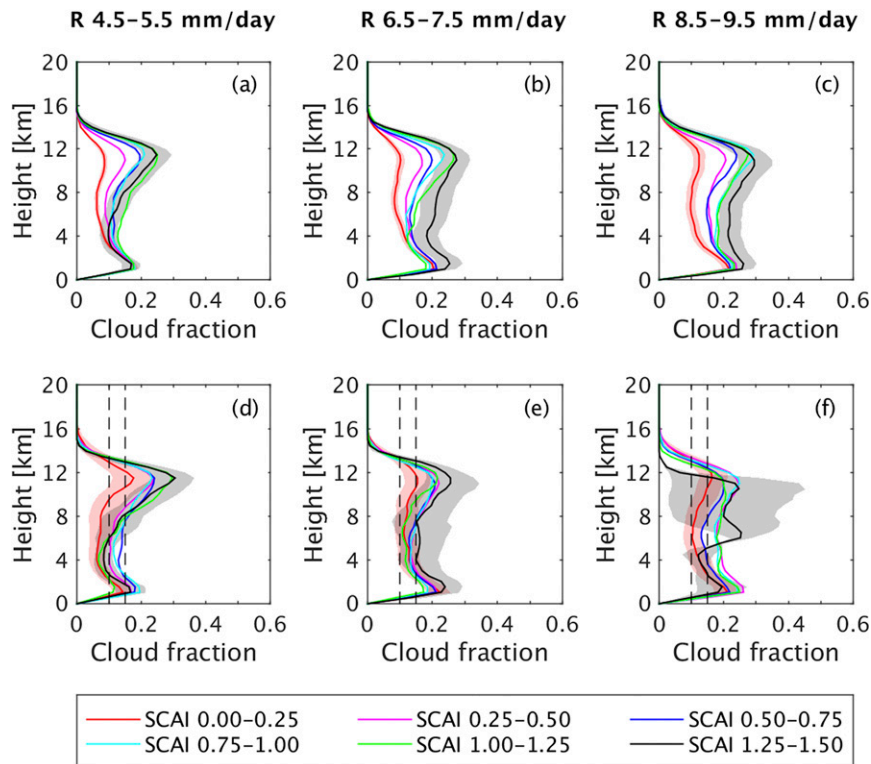


FIG. 4. As in Fig. 3, but only considering *CloudSat* observations to exclude cirrus and optically thin anvil.

water contents and optically thin cirrus, respectively, that can only be observed by the lidar. When we restrict observations to CCA between 0.10 and 0.15 in Figs. 4d–f, cloud fraction around 12 km is still significantly greater than CCA for several SCAI curves, for instance, indicated by the 90% confidence interval for the highest SCAI range. In the next section we discuss possible meteorological mechanisms behind the high fraction of optically thin anvil when convection is disaggregated.

5. Cloud-type frequency

The previous analysis groups all cloud and rainfall together, which masks the contribution from individual cloud types, as well as possible correlations between cloud types and SCAI or R . In Fig. 5 we show the mean cover from different cloud types versus SCAI, for three ranges of R (columns). The fractional cover shown is the bootstrapped mean for every 0.05 step in SCAI, considering all stretches within a range of 0.25 in SCAI and requiring at least 30 stretches; the rank correlation was then calculated using these bootstrapped means. The overlap of neighboring SCAI bins introduces correlation between consecutive means, but the wider range allows for smaller confidence intervals in the

cloud cover means. We note that our conclusions based on rank correlation—particularly in terms of sign of the correlation and the statistical significance—are not affected by this choice of overlapping bins.

We see in Figs. 5a–c that cirrus and anvil generally increase when SCAI increases, whereas clear-sky fraction and low-level clouds (Figs. 5j–l) decrease. These relationships all have a significant Spearman rank correlation (which is provided in Table A1; correlation with SCAI, all CCA, final column); the correlations between cirrus and SCAI and between anvil and SCAI is positive, whereas the correlation between clear-sky fraction and SCAI and low-level clouds and SCAI is negative. For midlevel clouds and congestus (Figs. 5d–f), we cannot discern a monotonic increase or decrease and the correlations are not significant across all R . Deep stratiform clouds increase when SCAI increases (Figs. 5g–i), while deep convective clouds decrease, both with statistically significant rank correlations across all R , although the change in deep convective cover with SCAI is difficult to discern in Fig. 5. These results confirm the findings from Fig. 3, with the added understanding that the increase in cloudiness when SCAI increases is largely associated with more widespread optically thin anvil. Since these optically thin clouds typically do not contribute to CCA,

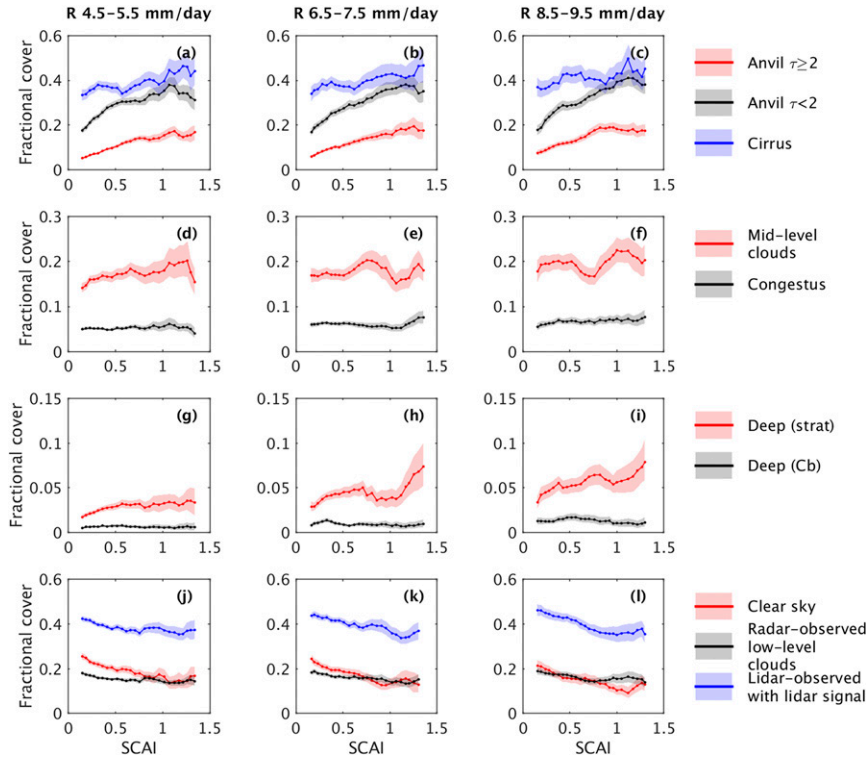


FIG. 5. Average fractional cover vs SCAI for a given R range. Shaded regions indicate the 90% confidence interval. (a)–(c) Anvil clouds and cirrus (τ stands for optical thickness), (d)–(f) midlevel clouds and congestus, (g)–(i) deep stratiform and deep convective (Cb), and (j)–(l) clear-sky and low-level clouds. Note that the range in fractional cover (y axis) changes with each row.

their abundance might explain why cloud fraction at 13 km is considerably greater than CCA in Figs. 3d–f.

As discussed in section 4, any relationship between cloud-type fractional cover and SCAI may be influenced by the correlation between SCAI and CCA and the correlation between a given cloud-type cover and CCA. We therefore continue our analysis by studying the relationship between cloud-type cover and CCA at constant SCAI. In Fig. 6 we show the fractional cover from different cloud types versus CCA, for three ranges of R (columns) and three ranges of SCAI (individual curves); the SCAI values separating the ranges were chosen to allow sufficient *CloudSat*–*CALIPSO* samples in each SCAI range for the different R . For given R and SCAI ranges, the bootstrapped mean cloud-type cover was calculated for every 0.01 step in CCA for all stretches within a range of 0.05 in CCA, and we set a minimum requirement of 30 stretches; the rank correlation was then calculated using these bootstrapped means (see Table A1, correlation with CCA). The rank correlation between cloud-type cover and SCAI was also calculated for each tercile of CCA values (see Table A1, correlation with SCAI).

Optically thick anvil cover strongly increases when CCA increases (Figs. 6a–c), which is expected given the relationship between anvil optical thickness and probability of brightness temperature below 240 K discussed in section 3. The correlation between optically thick anvil and CCA is 1.0 for the three R values shown (see Table A1), while the correlation with SCAI is also positive and statistically significant. For many CCA values, the 90% confidence intervals overlap with other SCAI curves (e.g., at CCA = 0.1 in Fig. 6b), which indicates that the strong correlation between thick anvil cover and SCAI is partly a consequence of the correlations between SCAI and CCA and between thick anvil cover and CCA.

Optically thin anvil cover also increases when CCA increases (Figs. 6d–f), but it has a strong relationship with SCAI that cannot be explained solely by the correlation between SCAI and CCA. The rank correlation between thin anvil and SCAI is greater than 0.90 for the R ranges and is greater than 0.88 for any given CCA range. For a given CCA range, the mean optically thin anvil cover for a given SCAI range is typically outside the 90% confidence interval for the other SCAI ranges and means can be separated by as much as 0.15 (or 75%

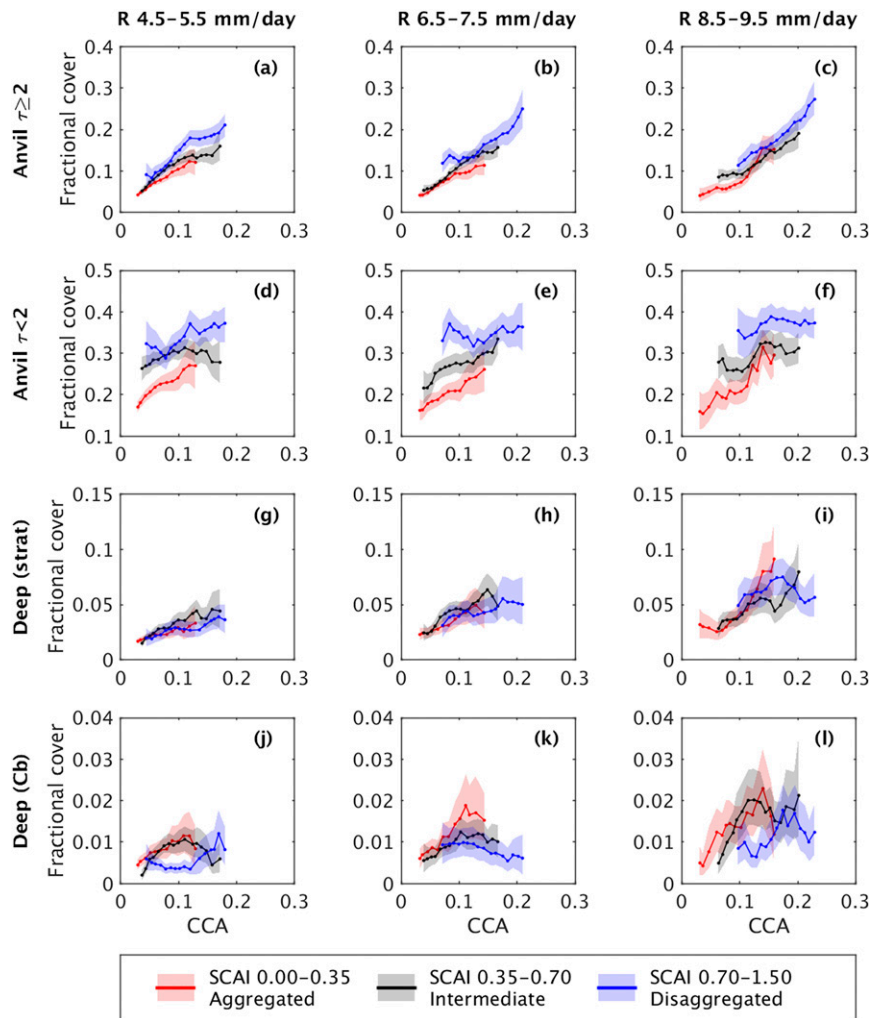


FIG. 6. Average fractional cover vs CCA for a given R range and for SCAI between 0.00 and 0.35 (red), SCAI between 0.35 and 0.70 (black), and SCAI between 0.70 and 1.50 (blue); τ stands for optical thickness. Shaded regions indicate the 90% confidence interval. (a)–(c) Thick anvil, (d)–(f) optically thin anvil, (g)–(i) deep (stratiform), and (j)–(l) deep (Cb) (i.e., convective). Note that the range in fractional cover (y axis) changes with each row.

in relative terms). Furthermore, we note that while thick anvil appears to reduce toward zero when CCA decreases, thin anvil cover is much greater than zero at low CCA. The presence of thin anvil clouds when CCA is low could be the result of long-lived remnants of thicker anvils that have precipitated out or sublimated to persist as optically thin layers, or of cirrus that has descended to a base below 200 hPa (Nair et al. 2012).

The greater abundance of anvil clouds when convection is disaggregated supports the concept of lower precipitation efficiency in this situation compared to aggregated convection. There are numerous ways to define precipitation efficiency, for instance through tracking Lagrangian particles (Langhans et al. 2015), or by studying the cloud microphysics budget or the

moisture budget (Sui et al. 2007). Here, we interpret precipitation efficiency of a convective cloud as the ratio of rainwater over the moisture source (Sui et al. 2007), where we define the moisture source as the amount of water vapor that leaves the boundary layer in convective updrafts. For disaggregated convection, the combination of high column-water vapor, overall greater cloudiness, and extensive anvil suggests that the combined efficiency of the convective clouds is low compared to an aggregated state of convection with similar R and CCA.

The fractional cover from deep stratiform profiles (Figs. 6g–i) has significant positive rank correlations with both SCAI and CCA. For this cloud type, however, for a given CCA, the correlation with SCAI is typically not statistically significant, which is illustrated by the

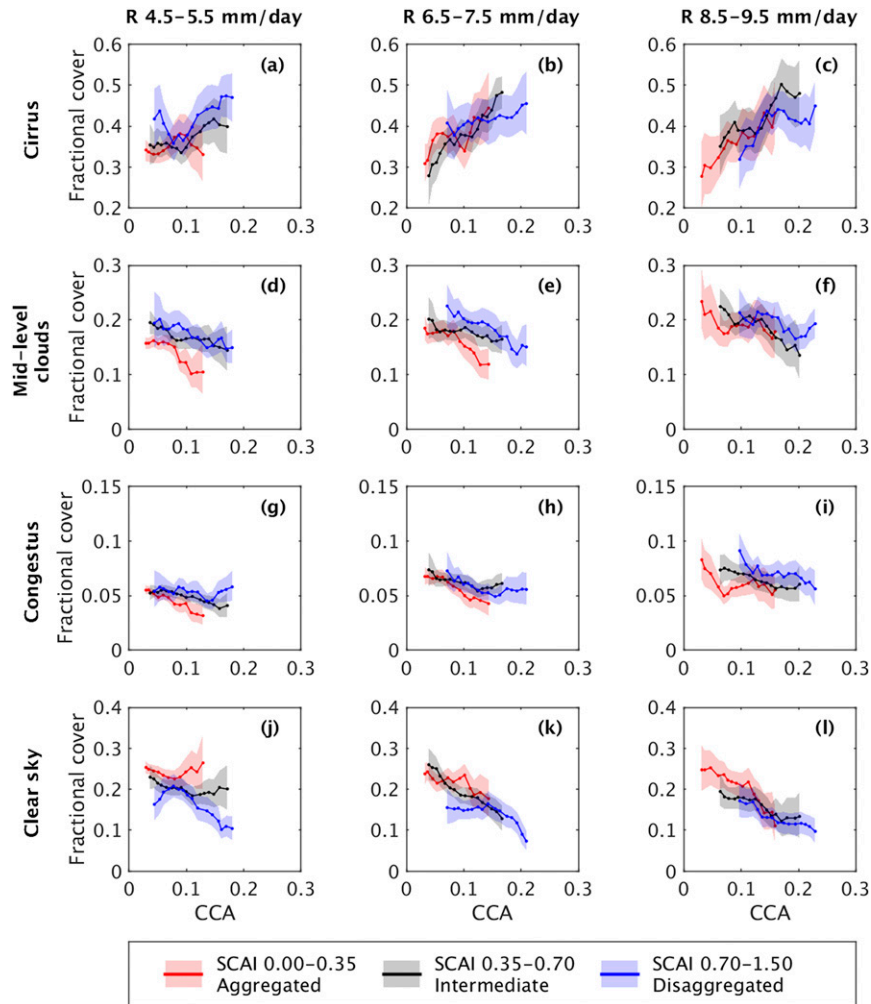


FIG. 7. As in Fig. 6, but for (a)–(c) cirrus, (d)–(f) midlevel clouds, (g)–(i) congestus, and (j)–(l) clear sky.

consistent overlap of the 90% confidence intervals with other curves.

The cover from deep convective profiles [Figs. 6j–l, indicated as Deep (Cb)] has a positive correlation with CCA, but this is only statistically significant for the low SCAI range. In contrast, the correlation with SCAI is negative (see also Fig. 5), but it is not always significant for all CCA ranges, as evident from the overlap between mean cover and 90% confidence intervals for different SCAI ranges. This lack of a strong relationship with SCAI or CCA supports the idea of Craig (1996) that the total area of convective updrafts should be roughly proportional to the large-scale forcing in a region, which in our analysis we assume to be in balance with, and therefore equivalent to, the mean precipitation rate R .

In Fig. 7, we show the fractional cover against CCA for the remaining cloud types and for clear-sky conditions.

Cover from cirrus does not show a consistent relationship with SCAI, while it has a significant positive correlation with CCA for all R ranges, even when considering individual SCAI ranges. However, for most SCAI and R ranges, we note that for a change in CCA of 0.1, the change in mean cirrus cover is less than half the 90% confidence interval. The lack of variation of cirrus cover with SCAI, CCA, and even R may be due to formation mechanisms that are not related to local convective activity. For instance, cirrus can be generated through gravity waves and Kelvin waves thousands of kilometers away (e.g., ahead of the MJO; Virts and Wallace 2010) or through radiatively driven large-scale ascent in the tropical tropopause layer.

We note that the rank correlation between midlevel clouds and CCA is negative, whereas its correlation with SCAI is positive (when it is significant). This positive

correlation with SCAI can be identified in Figs. 7d–f and, for various CCA ranges, the mean cover for a given SCAI range is outside the 90% confidence intervals for the other SCAI ranges. In contrast, the positive correlation with SCAI was difficult to discern in Fig. 5, seemingly due to the positive correlation between SCAI and CCA and the correlations of opposite sign between midlevel clouds and CCA and between midlevel clouds and SCAI. The increase in midlevel cloud cover when SCAI increases coincides with increases in thick and thin anvil, but the decreasing cover when CCA increases is surprising. The latter will require further investigation into the microphysical and macrophysical structure of midlevel clouds and whether these clouds are often missed by the radar, for instance due to having little or no ice present (Zhang et al. 2010).

Congestus shows a clear increase with R (approximately 50% between the lowest and highest R) but no consistent relationship with SCAI. Across all R and also for any given SCAI range, congestus decreases when CCA increases, associated with a decrease in midlevel clouds. Midlevel clouds can be generated through detrainment near the freezing level (Johnson et al. 1999) from both deep convection and congestus. Thus, for a given CCA, when convection is disaggregated, more individual convective plumes can mix with the environment and produce midlevel clouds through detrainment, which might explain the increase in midlevel clouds when SCAI increases. The decrease in midlevel cloud when CCA increases could therefore be a result of the decrease in congestus, but the physical mechanism for the latter is not obvious from these statistical relationships alone.

In Figs. 7j–l we show the fraction of profiles without any cloud layers, denoted as clear sky. This fractional cover decreases with CCA as we might expect, although when convection is aggregated (red curves), this decrease does not vary beyond the 90% confidence interval. Clear sky also become less frequent as SCAI increases, consistent with results using ISCCP (Tobin et al. 2013). However, for any given CCA range, we note that a change from aggregated to disaggregated convection does not lead to a decrease in clear-sky fraction beyond the 90% confidence interval. Tobin et al. (2013) found that low SCAI is associated with a dry mid-troposphere and they related this to the proposed mechanism through which convective aggregation promotes a larger coverage of large-scale subsidence (Muller and Held 2012), both of which in the tropics may lead to widespread low-level stratocumulus or trade cumulus. We briefly investigate several combinations of cloud types and clear sky to estimate the fractional coverage of cloud regimes that could be expected in

regions with large-scale subsidence, to test whether this fractional coverage decreases when SCAI increases.

First, we test whether this lack of significant decrease of clear-sky cover when CCA or SCAI increase is due to an associated decrease of low-level clouds. For instance, while an increase in CCA or SCAI is evidently associated with more anvil, which would reduce clear-sky fraction, it may also be associated with fewer low-level clouds (investigated in section 6), which would increase clear-sky fraction. In Figs. 8a–c we see that the fractional cover of clear-sky profiles and profiles with only low-level clouds decreases when CCA or SCAI increases. When restricting the range of SCAI or CCA, respectively, the rank correlations are negative and typically statistically significant, and we note that the curves vary beyond the 90% confidence intervals for the two lower rain rates considered. Compared to the low SCAI range, the fractional area of clear sky and low-level clouds (and no other clouds) is 0.10 smaller for the high SCAI range and a similar decrease in low-level cloud cover can be noted when CCA increases. This result supports the idea that convective aggregation promotes widespread clear sky and low-level cloud.

Second, we test if cirrus has an impact on the fractional area of clear sky and its relationship with SCAI and CCA, without low-level clouds (Figs. 8d–f) and with low-level clouds (Figs. 8g–i). Cirrus is abundant across all SCAI and CCA ranges considered, but it does not have a significant relationship with SCAI and its relationship with CCA is not consistent across SCAI and R ranges. Furthermore, formation mechanisms for cirrus have been proposed that do not rely on local convective activity, so that the presence of cirrus—and its negation of clear sky—may sometimes be random and not correlated with SCAI or CCA. In Figs. 8d–f, when clear sky is combined with cirrus, we note that the relationship with CCA and SCAI is similar compared to the clear-sky fraction in Figs. 7j–l, apart from an overall increase in fractional cover. However, the combined fractional cover of clear sky, low-level clouds, and cirrus, shown in Figs. 8g–i, decreases significantly when SCAI or CCA increases. This decrease in fractional area is greater than when clear sky is combined with low-level clouds alone and the curves for individual SCAI ranges are clearly separated beyond their 90% confidence intervals. We conclude that, regardless of cirrus, the fractional cover of low-level clouds and clear sky can increase by as much as 0.2 (50% in relative terms) when convective aggregation increases.

6. Low-level cloud cover

Estimating low-level cloud cover from satellite data is not straightforward, as observations of low-level clouds

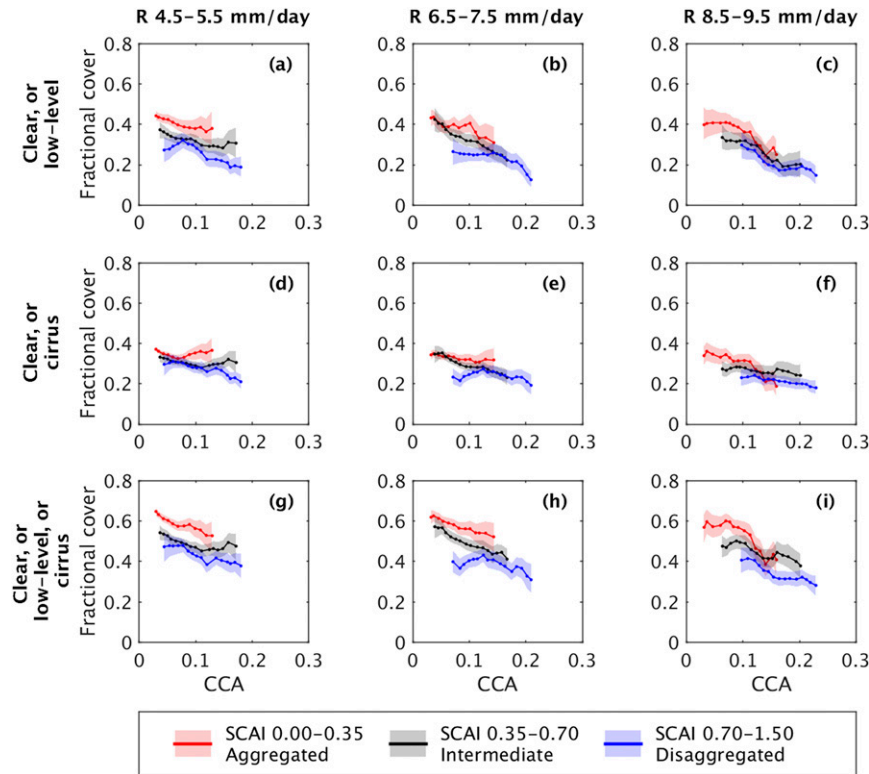


FIG. 8. As in Fig. 6, but for (a)–(c) profiles with clear sky or low-level clouds only, (d)–(f) profiles with clear sky or cirrus only, and (g)–(i) profiles with clear sky or cirrus and/or low-level clouds.

are incomplete. The *CloudSat* radar sensitivity threshold means that it only detects low-level clouds with high liquid water contents or when drizzle is present (Christensen et al. 2013b). In our analysis, for profiles where *CALIPSO* detects low-level cloud layers, only 40% of these profiles have low-level cloud layers that are also detected by *CloudSat*, so the low-level cloud cover estimated from radar alone will be an underestimate. The *CALIPSO* lidar, on the other hand, gets attenuated by thick clouds—typically optical thickness greater than 3 (Chepfer et al. 2008)—so that for cloudy conditions, the probability of detecting low-level clouds using *CloudSat*–*CALIPSO* is severely reduced.

Here, we present the “lidar-observed low-level cloud fraction with lidar detection” as our best estimate for low-level cloud cover over tropical ocean. We consider a profile to have “lidar detection” if the *CALIPSO* signal is not attenuated at 3.5 km above mean sea level (approximately the 700-hPa level), based on the *CALIPSO* vertical feature mask (Anselmo et al. 2006). To substantiate our choice for best low-level cloud estimate, we hypothesize that for a given SCAI–*R* combination, low-level clouds are equally likely to occur in profiles with lidar detection and in profiles without lidar detection

(i.e., without and with thick cloud aloft, respectively), and we assume that low-level clouds are not systematically different in their microphysical composition and macrophysical structure depending on their location. Under these conditions, the following two fractions should be approximately equal:

- 1) The fraction of low-level cloud profiles with *CloudSat* radar detections over all profiles with lidar detection.
- 2) The fraction of low-level cloud profiles with *CloudSat* radar detections over all profiles without lidar detection.

From Fig. 9a we see that, indeed, these two fractions are comparable, although the radar-observed low-level cloud fraction without lidar detection (open symbols) appears consistently slightly smaller. Notably, the radar-observed fraction with lidar detection (filled symbols) provides a reasonable estimate of the all-sky radar-observed low-level cloud fraction, as indicated by the dashed line. We have no means of testing our assumption on the cloud microphysical and macrophysical structure, but we can analyze whether low-level cloud structures vary between different SCAI–*R*

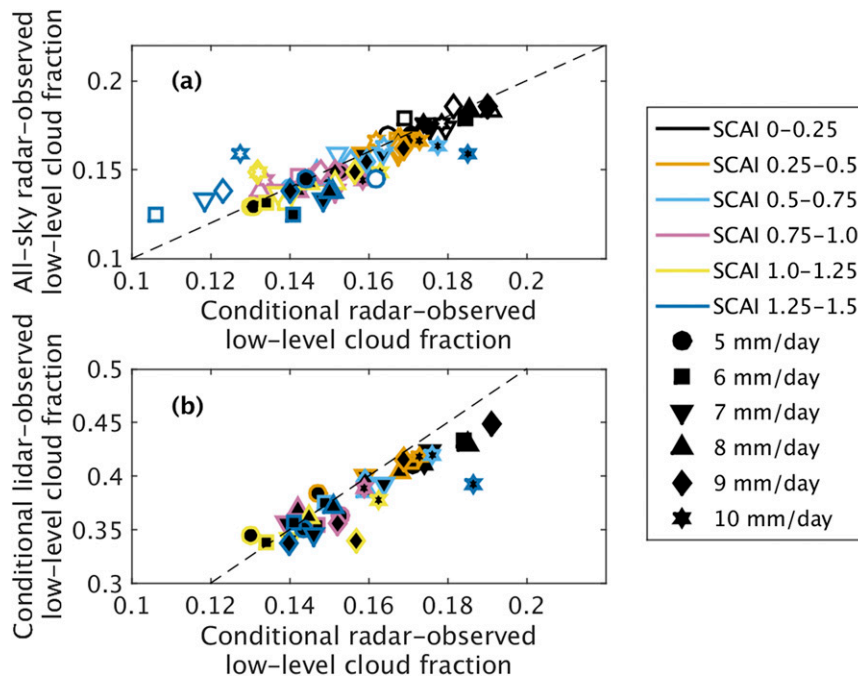


FIG. 9. (a) Radar-observed low-level cloud fraction for different SCAI- R combinations, indicated by colors and symbols, respectively. Filled symbols are for low-level cloud fraction conditional on a lidar signal down to 3.5 km; open symbols are conditional on the lidar being attenuated. Dashed line indicates a 1:1 ratio between conditional fraction and all-sky fraction. (b) Low-level cloud fraction conditional on a lidar signal down to 3.5 km, as observed by radar vs as observed by lidar. Line indicates the 1:2.5 ratio.

combinations by comparing the probability of detection by *CloudSat* in Fig. 9b. We note that the lidar-observed fraction is approximately 2.5 times greater than the radar-observed fraction and that this ratio does not vary consistently with SCAI or R . Thus, the probability of low-level cloud detection by the radar is not affected by the large-scale conditions represented by the different SCAI- R combinations. Because the probability of detection of low-level clouds by *CloudSat* does not vary much across SCAI- R ranges (Fig. 9b), we believe that our assumption on low-level cloud microphysical composition and macrophysical structure is supported (though not proven).

In Fig. 10 we show the cloud cover from low-level clouds as it is defined from these different combinations of the *CloudSat*-*CALIPSO* observations. For all definitions of low-level cloud cover, a decrease is noticeable as SCAI increases, while cover also decreases when CCA increases. The factor 2.5 increase in low-level cloud between the radar and the lidar (with lidar signal) is evident across all R and SCAI combinations (Figs. 10a-c,g-i). For the “lidar-observed all-skies” cover (Figs. 10d-f), the rank correlation is negative both for SCAI and for CCA and is typically statistically significant when restricting the range of CCA or SCAI,

respectively. More CCA leads to relatively less low-level cloud detection due to lidar attenuation, which would explain this strong decrease when CCA increases. For many CCA values, curves for different SCAI ranges do not overlap with other 90% confidence intervals, but this apparent relationship with SCAI could be due to other cloud types (or multilayered clouds) attenuating the lidar signal. Thus, we continue our discussion by considering our best estimate of low-level cloud cover (i.e., lidar observed with lidar signal).

Our best estimate does not vary consistently with CCA across the SCAI- R ranges (Figs. 10g-i) and no consistent sign in rank correlation is found. For a given CCA range, low-level cloud cover decreases when SCAI increases—statistically significant for all but one of the R and CCA combinations tested—with a typical difference of 0.05–0.10 between the low and high SCAI ranges (approximately 15% in relative terms.). Thus, when we account for the low-level clouds obscured by optically thick clouds, our results continue to support the suggestion by Tobin et al. (2013) that low-level cloud formation depends on the large-scale thermodynamic and dynamic conditions that correlate with convective aggregation.

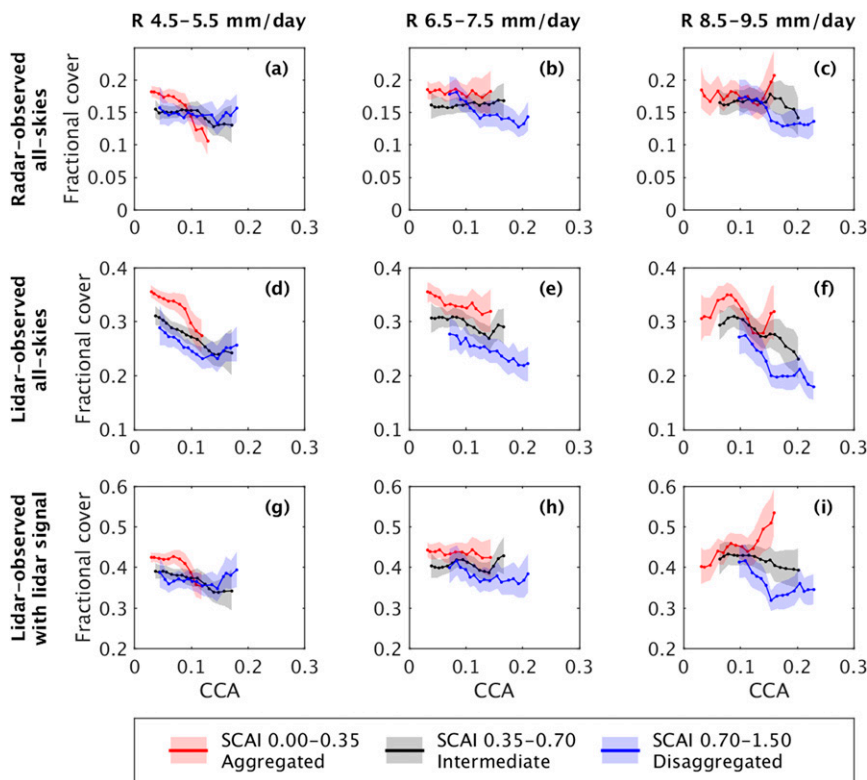


FIG. 10. As in Fig. 6, but for (a)–(c) radar-observed low-level clouds for all sky conditions, (d)–(f) lidar-observed low-level clouds for all sky conditions, and (g)–(i) lidar-observed low-level clouds for sky conditions with a lidar signal at 3.5 km.

7. Discussion

Further insight into the results of this study can be gained from examining how the relationships between convective aggregation and cloud types vary with SST. Indeed, models suggest that convective aggregation is sensitive to surface temperature (e.g., Wing and Emanuel 2014; Wing and Cronin 2016; Coppin and Bony 2015; Holloway and Woolnough 2016). Igel et al. (2014) and Zelinka and Hartmann (2010) suggest that the anvil cloud amount decreases as the SST increases, but whether or not this decrease is associated with an increase of convective aggregation remains unknown. Therefore we briefly consider how convective aggregation—and its relationship to different cloud types—changes with SST (for the same domain-averaged precipitation rate and large-scale vertical motion). We follow the same methodology as is used throughout the paper, changing only the range of SSTs, but having the same range of $\omega \pm 1$ standard deviation calculated for 301 K.

In Fig. 11 we show the RLH fraction for rainfall rates between 4.5 and 5.5 mm day⁻¹ and for SST ranges of 299.5–300.5 K, 301.5–302.5 K, and 302.5–303.5 K, for comparison with Figs. 3a and 3d. The increase in

cloudiness when SCAI increases is universal across the different SST ranges, while for a given SCAI there is an obvious dependence of cloudiness on SST as well: the height of maximum cloud fraction increases from 12–13 km at 300 K to 14–15 km at 303 K. Assuming that the “fixed-anvil temperature” hypothesis (Hartmann and Larson 2002) or the “proportionally higher anvil temperature” hypothesis (Zelinka and Hartmann 2010) applies, the rise of high clouds when SST increases is associated with a nearly unchanged cloud-top temperature or a slight warming. Igel et al. (2014), however, studied individual contiguous cloud objects identified in *CloudSat* data and found cooler cloud-top temperatures with warmer SSTs. A direct comparison between our results and those studies is not straightforward, since we consider variations of cloud types with SST for a given domain-averaged precipitation rate and a given vertical motion, whereas Igel et al. (2014) and Zelinka and Hartmann (2010) do not stratify their results by precipitation.

In Fig. 12, we show the fractional cover of thick and thin anvil, cirrus, and our best estimate of low-level cloud amount. We see that for the different SST ranges, thick anvil is strongly associated with CCA but not with SCAI (for a fixed CCA), whereas thin anvil does have a

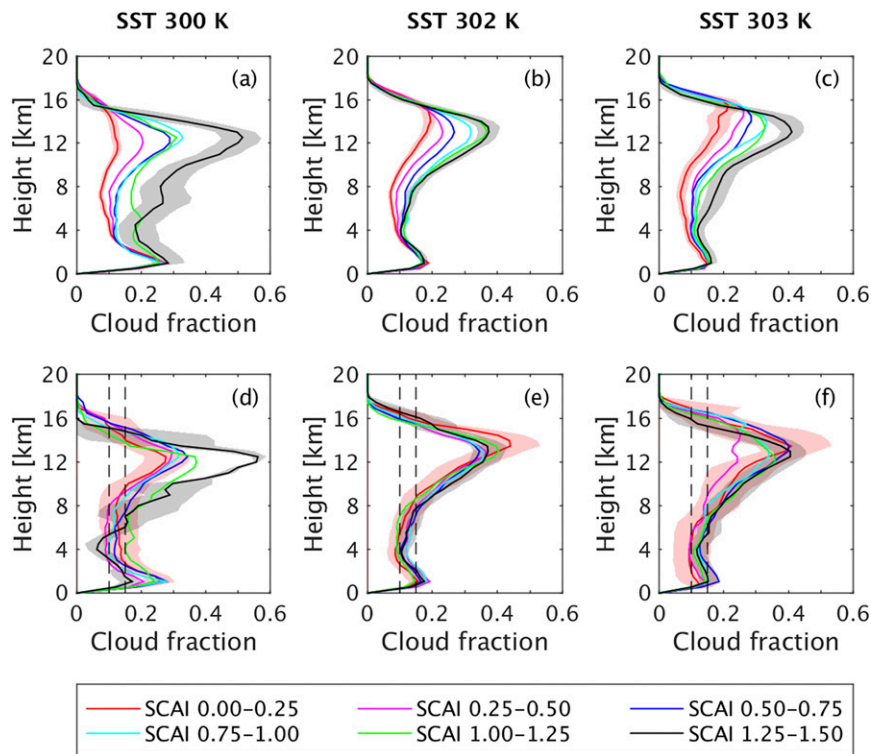


FIG. 11. As in Fig. 3, but for rainfall rates between 4.5 and 5.5 mm day^{-1} and for SST ranges of (a),(d) 299.5–300.5 K, (b),(e) 301.5–302.5 K, and (c),(f) 302.5–303.5 K.

strong association with SCAI, becoming more prominent when convection is disaggregated, as we found in Figs. 6a and 6d. Cirrus cover does not show a clear association with SCAI or CCA for any of the SST ranges considered, but it does strongly increase with warmer SSTs. Note, however, that our use of a fixed pressure level to distinguish cirrus from anvil clouds is likely associated with different heights at different SSTs and therefore this result requires some caution; further work may focus on the cloud-top and cloud-base heights of all optically thin ice cloud, for instance.

Igel et al. (2014) found a decreasing anvil width per cloud object when SST increases, but for a given SCAI, CCA, and rainfall rate, we do not see a clear response in total fractional cover of anvil cloud with varying SST. However, we do note that in our analysis, at lower SSTs, low SCAI values are more frequently observed, whereas at higher SSTs high SCAI values are more frequently observed. Thus, if high SSTs in observations are more frequently associated with disaggregated convection, they will also be associated with a larger number of individual clusters [incidentally, Igel et al. (2014) report a much greater number of cloud objects for higher SSTs]. The decreasing anvil width when SST increases may thus be partly due to convection being less aggregated in the

observations, although further investigation is required to confirm this suggestion.

Finally, in Figs. 12j–l, we consider low-level cloud amounts using our best estimate. We still note significant negative rank correlations between low-level cloud cover and SCAI for most CCA ranges (not shown), but we see that the mean fractional cover for a given SCAI range typically lies within the 90% confidence interval of the other SCAI ranges. Thus, the decrease in low-level cloud cover when convection becomes less aggregated is not consistent across different SST regimes. Instead, we note a strong association between low-level cloud cover and varying SSTs, as for a CCA of 0.1 the fractional cover decreases from around 0.45 for SSTs around 300 K to around 0.25 for SSTs around 303 K. This is surprising, as Johnson et al. (1999) found an increasing frequency of cumulus clouds over warmer SSTs, although we note that in their observations there was an absence of deep convective clouds in those situations. Alternatively, the decrease in low-level cloud cover may be directly related to the increase in cirrus cover, since a decrease of the radiative cooling rate of the planetary boundary layer leads to a weaker inversion, which in turn relates to a reduction in low-level cloud cover (Wood and Bretherton 2006). A positive feedback has been argued for low-level

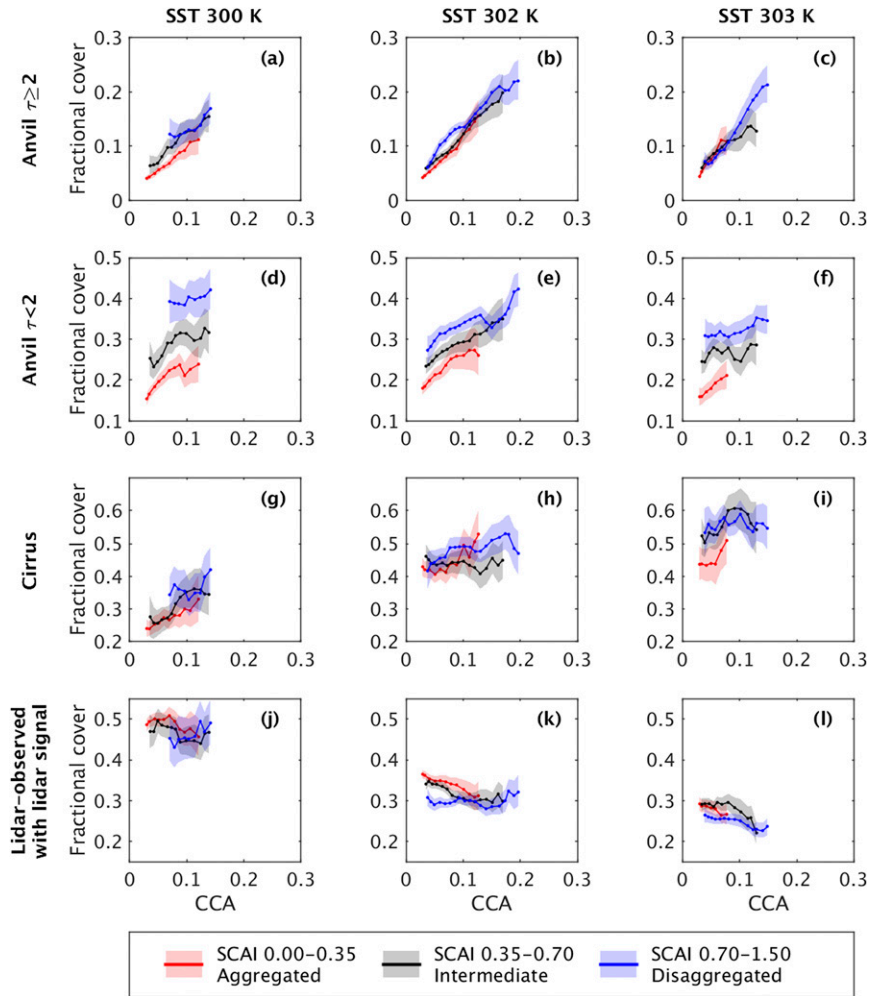


FIG. 12. As in Fig. 6, but for rainfall rates between 4.5 and 5.5 mm day^{-1} and for SST ranges of (left) 299.5–300.5 K, (middle) 301.5–302.5 K, and (right) 302.5–303.5 K, for (a)–(c) thick anvil, (d)–(f) optically thin anvil, (g)–(i) cirrus, and (j)–(l) lidar-observed low-level clouds for sky conditions with a lidar signal at 3.5 km.

cloud cover over tropical ocean due to a weakening of the inversion (e.g., Qu et al. 2015), but these studies were primarily focused on the large-scale subsidence regions in the tropics. Nevertheless, it will be a worthwhile endeavor to use a similar modeling framework to study the relationship between low-level cloud characteristics and the large-scale environment in simulations with high R and significant presence of deep convection.

8. Conclusions

Using 5 years of *CloudSat*–*CALIPSO* data, we have shown that, over tropical ocean, the vertical structure of clouds is related to the degree of convective aggregation. The degree of convective aggregation is determined using SCAI, the Simple Convective Aggregation Index (Tobin

et al. 2012), which in our analysis ranges from 0 for aggregated convection to 1.5 for disaggregated convection. Changes in convective aggregation are primarily associated with changes in two cloud types: anvil clouds and low-level clouds. Cloud fraction changes monotonically with SCAI at all heights between 3 and 14 km, with the largest change at 13 km from 0.15 at aggregated convection to 0.38 at disaggregated convection. Our results clearly show that the vertical cloud distribution is associated more strongly with SCAI than with the mean rainfall rate.

We have taken into account the fact that SCAI is positively correlated with cold cloud area (CCA), from which it is derived and which itself is a measure of high-level cloud fraction. Thus, the large increase of cloud fraction with SCAI around 13-km height is mostly due to the increase of CCA with SCAI, as illustrated when our

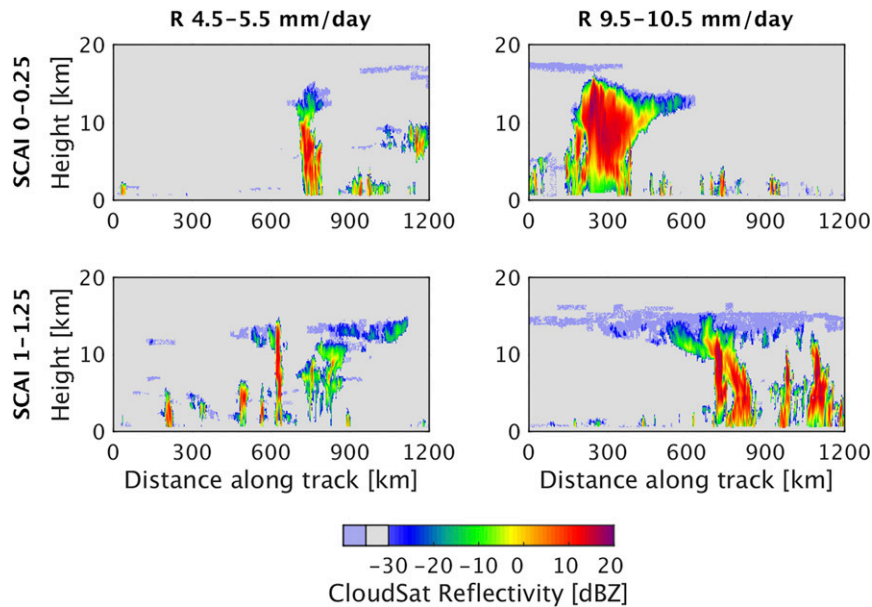


FIG. 13. *CloudSat* reflectivities (main color bar) and *CALIPSO* cloud mask (light blue color at left of color bar) for four SCAI-*R* combinations. Quicklooks are selected based on whether fractional cover from the following cloud-types is representative of the SCAI-*R* combination: thin anvil cloud, thick anvil cloud, precipitating cloud (which is the total of congestus, deep convective, and deep stratiform), and clear sky.

findings are restricted by CCA, and as shown similarly for fractional cloud cover of thick anvil. Although this result may seem obvious, this is still an important point, since different SCAI/CCA regimes, for a given rain rate, have different amounts of moisture and cloudiness, and have different amounts of various cloud types. We can confirm that CCA is comparable to—although slightly less than—the combined fractional cover from thick anvil and deep precipitating clouds (not shown).

Our results show that the fractional cover of optically thin anvil increases when CCA increases—while the thin anvil are not part of CCA—indicating that these clouds are closely associated with deep convection, likely due to detrainment. However, thin anvil shows a much stronger association with SCAI than with CCA, increasing from around 0.2 in aggregated conditions to around 0.4 when convection is disaggregated. Cirrus clouds, which have cloud base above the 200-hPa level, increase their fractional cloud cover with SCAI and with CCA, but the increase stays within the 90% confidence interval. The lack of a strong relationship between cirrus and SCAI or CCA is consistent with cirrus formation mechanisms independent of convection and convective aggregation (e.g., large-scale tropical waves).

The typical variation of clouds with aggregation and precipitation is illustrated in Fig. 13, which shows selected quicklooks of *CloudSat* reflectivity profiles and *CALIPSO* cloud mask. The quicklooks describe what the different aggregation states, for the same rain rate or

large-scale forcing, look like on average: a comparable fraction of deep convective profiles with different amounts of anvil, shallow clouds, and clear-sky.

Our study thus suggests that the distribution of cloud types and vertical cloud fraction are strongly affected by the degree of aggregation of deep convection. In particular, we observe a clear reduction of the anvil cloud amount in more aggregated situations. Several physical interpretations might be given to this behavior. It could be related to an increase of the precipitation efficiency of convective systems: as the convective cells aggregate, they become surrounded by moister air, which reduces the entrainment of unsaturated environmental air into the clouds and reduces the re-evaporation of the falling rain. Another interpretation as recently proposed by Bony et al. (2016) is that aggregated convection warms the troposphere and increases upper-tropospheric stability, which in turn reduces convective outflow and could therefore relate to a reduction in anvil cloud amount. The future investigation of covariations between convective aggregation, the different cloud types studied here and thermodynamic parameters could help test this hypothesis. The interpretation of the increase of low-level clouds with increased aggregation will also merit further investigation. Whether it results from the reduced upper-level cloud amount and the subsequent reduced downward infrared radiation (Christensen et al. 2013a) or from more dynamical influences remains an open question.

TABLE A1. Spearman rank correlation of the bootstrapped means of fractional cloud cover for the types considered in the manuscript (in order of appearance), vs CCA and SCAI, restricting the range of SCAI and CCA, respectively, and for rainfall rate. Only statistically significant values are shown, where statistical significance indicates less than 5% chance of no correlation. Negative correlations are indicated in bold.

Type	R (mm day ⁻¹)	Corr. w/CCA				Corr. w/SCAI			
		SCAI tercile			All	CCA tercile			All
		Lower	Middle	Upper		Lower	Middle	Upper	
Anvil $\tau \geq 2$	5	1.0	0.99	0.99	1.0	0.91	0.86	0.96	0.97
	7	0.99	0.99	1.0	1.0	0.92	0.94	0.97	0.98
	9	0.99	0.94	1.0	1.0	0.90	0.78	0.89	0.82
Anvil $\tau < 2$	5	0.89	0.86	0.80	0.99	0.90	0.88	0.93	0.90
	7	0.99	0.97	0.54	0.96	0.97	0.99	0.90	0.94
	9	0.96	—	0.60	0.81	0.98	0.89	0.93	0.97
Deep (strat)	5	0.96	0.97	0.85	0.94	0.60	—	0.48	0.87
	7	0.95	0.87	0.98	0.97	—	—	—	0.56
	9	0.90	0.79	—	0.88	—	—	—	0.87
Deep (Cb)	5	0.99	—	0.87	0.51	-0.61	-0.7	-0.83	-0.41
	7	0.92	—	—	—	—	-0.65	-0.85	-0.56
	9	0.77	—	0.75	0.90	—	-0.57	—	-0.58
Cirrus	5	—	0.93	0.81	0.98	-0.58	—	0.69	0.88
	7	0.76	0.99	0.99	0.97	—	0.58	—	0.86
	9	0.97	0.77	0.71	0.93	0.63	—	-0.74	0.7
Midlevel clouds	5	-0.93	-0.89	-0.87	-0.95	0.59	0.87	0.75	0.71
	7	-0.86	-0.89	-0.86	-0.96	—	0.93	0.56	—
	9	-0.61	-0.88	-0.63	-0.86	—	—	0.85	0.51
Congestus	5	-0.90	-0.88	-0.78	-0.57	0.7	—	0.57	—
	7	-0.97	-0.72	-0.86	-0.79	0.62	0.59	-0.47	—
	9	—	-0.97	-0.88	-0.86	0.81	0.79	0.77	0.8
Clear sky	5	—	-0.94	-0.98	-0.99	—	-0.75	-0.90	-0.95
	7	-0.79	-1.0	-0.85	-0.99	—	-0.98	-0.58	-0.91
	9	-0.97	-0.84	-0.95	-0.98	-0.87	-0.61	—	-0.90
Clear, or low-level	5	—	-0.95	-0.98	-1.0	-0.63	-0.88	-0.94	-0.96
	7	-0.85	-1.0	-0.90	-1.0	—	-0.98	-0.87	-0.93
	9	-0.90	-0.92	-0.86	-0.99	-0.88	-0.69	-0.55	-0.91
Clear, or cirrus	5	—	-0.66	-0.93	-0.99	-0.96	-0.85	-0.94	-0.91
	7	-0.84	-0.98	-0.75	-0.99	—	-0.94	-0.66	-0.95
	9	-0.96	—	-0.97	-1.0	-0.74	-0.79	-0.64	-0.92
Clear, or low-level or cirrus	5	—	-0.96	-0.82	-1.0	-0.94	-0.91	-0.96	-0.94
	7	-0.97	-0.99	-0.82	-1.0	-0.95	-0.99	-0.98	-0.99
	9	-0.86	-0.76	-0.95	-0.99	-0.78	-0.85	-0.98	-0.93
Radar-observed all-skies	5	-0.95	-0.67	—	-0.58	-0.78	-0.90	—	-0.79
	7	—	—	—	-0.88	-0.96	—	-0.81	-0.94
	9	—	—	-0.75	-0.83	-0.90	-0.60	-0.88	-0.70
Lidar-observed all-skies	5	-0.99	-0.98	-0.62	-0.81	-0.84	-0.97	-0.92	-0.94
	7	-0.87	-0.90	-0.92	-1.0	-0.99	-0.96	-0.96	-0.98
	9	—	-0.81	-0.94	-0.92	-0.93	-0.69	-0.98	-0.90
Lidar-obs. w/lidar signal	5	—	-0.92	—	-0.59	-0.69	-0.98	—	-0.76
	7	—	—	—	-0.94	-0.98	-0.84	-0.83	-0.94
	9	0.85	—	-0.69	-0.82	-0.95	-0.89	-0.96	-0.90

In any event, the systematic variations of cloud types with convective aggregation pointed out here imply that changes in convective aggregation are associated with significant changes in atmospheric cloud-radiative

effects. Indeed, low-level clouds radiatively cool the troposphere (especially the boundary layer), whereas anvil clouds radiatively warm the troposphere. Therefore, in situations where convection is more aggregated,

the reduced anvil cloud amount combined with the increased low-cloud amount in the vicinity of deep convection may promote the narrowing of convergence areas and the extension of subsiding areas, thus providing a positive feedback on convective aggregation. By modulating the atmospheric radiative cooling, changes in convective aggregation may also play an active role in the intraseasonal variability of the tropical atmosphere (Tobin et al. 2013; Arnold and Randall 2015).

A final open question is whether, as convective aggregation increases, the radiative impact of changes in the anvil cloud amount on the top-of-atmosphere budget is opposed, or instead amplified, by changes in the low-cloud amount. Answers to these questions will be required to assess the role that convective aggregation plays in climate and hydrological sensitivity (Mauritsen and Stevens 2015; Bony et al. 2015).

Acknowledgments. Official *CloudSat* products “2B-GEOPROF” and “ECMWF-AUX” are available at cloudsat.cira.colostate.edu and are provided by the NASA *CloudSat* project; *CALIPSO* lidar data are available at eosweb.larc.nasa.gov. The *CloudSat* and *CALIPSO* data were analyzed using the DARDAR merged products, which were accessed through the ICARE Data and Services Center, available from icare.univ-lille1.fr/projects/dardar. Sandrine Bony was supported by the European Research Council from the European Union (Grant Agreement 694768). Chris Holloway was funded by UK NERC Grant NE/I021012/1. The combined rainfall-CCA-SCAI dataset will be made available through the NERC Centre for Environmental Data Archival (CEDA) at catalogue.ceda.ac.uk.

APPENDIX

Table of Rank Correlations

Spearman rank correlations between cloud-type cover and CCA and SCAI (Table A1).

REFERENCES

- Allan, R., and B. Soden, 2008: Atmospheric warming and the amplification of precipitation extremes. *Science*, **321**, 1481–1484, doi:10.1126/science.1160787.
- Anselmo, T., and Coauthors, 2006: Cloud–Aerosol Lidar Infrared Pathfinder Satellite Observations (CALIPSO). NASA Langley Research Center Doc. PC-SCI-503, 100 pp. [Available online at http://www-calipso.larc.nasa.gov/products/CALIPSO_DPC_Rev2x4.pdf.]
- Arkin, P. A., and B. N. Meisner, 1987: The relationship between large-scale convective rainfall and cold cloud over the Western Hemisphere during 1982–84. *Mon. Wea. Rev.*, **115**, 51–74, doi:10.1175/1520-0493(1987)115<0051:TRBLSG>2.0.CO;2.
- Arnold, N. P., and D. A. Randall, 2015: Global-scale convective aggregation: Implications for the Madden–Julian oscillation. *J. Adv. Model. Earth Syst.*, **7**, 1499–1518, doi:10.1002/2015MS000498.
- Battaglia, A., J. M. Haynes, T. L’Ecuyer, and C. Simmer, 2008: Identifying multiple-scattering-affected profiles in *CloudSat* observations over the oceans. *J. Geophys. Res.*, **113**, D00A17, doi:10.1029/2008JD009960.
- Bony, S., and Coauthors, 2015: Clouds, circulation and climate sensitivity. *Nat. Geosci.*, **8**, 261–268, doi:10.1038/ngeo2398.
- , B. Stevens, D. Coppin, T. Becker, K. A. Reed, A. Voigt, and B. Medeiros, 2016: Thermodynamic control of anvil cloud amount. *Proc. Natl. Acad. Sci. USA*, **113**, 8927–8932, doi:10.1073/pnas.1601472113.
- Bretherton, C. S., P. N. Blossey, and M. Khairoutdinov, 2005: An energy-balance analysis of deep convective self-aggregation above uniform SST. *J. Atmos. Sci.*, **62**, 4273–4292, doi:10.1175/JAS3614.1.
- Chepfer, H., S. Bony, D. Winker, M. Chiriaco, J.-L. Dufresne, and G. Sèze, 2008: Use of *CALIPSO* lidar observations to evaluate the cloudiness simulated by a climate model. *Geophys. Res. Lett.*, **35**, L15704, doi:10.1029/2008GL034207.
- Christensen, M. W., G. G. Carrió, G. L. Stephens, and W. R. Cotton, 2013a: Radiative impacts of free-tropospheric clouds on the properties of marine stratocumulus. *J. Atmos. Sci.*, **70**, 3102–3118, doi:10.1175/JAS-D-12-0287.1.
- , G. L. Stephens, and M. D. Lebsock, 2013b: Exposing biases in retrieved low cloud properties from *CloudSat*: A guide for evaluating observations and climate data. *J. Geophys. Res. Atmos.*, **118**, 12 120–12 131, doi:10.1002/2013JD020224.
- Coppin, D., and S. Bony, 2015: Physical mechanisms controlling the initiation of convective self-aggregation in a general circulation model. *J. Adv. Model. Earth Syst.*, **7**, 2060–2078, doi:10.1002/2015MS000571.
- Craig, G. C., 1996: Dimensional analysis of a convecting atmosphere in equilibrium with external forcing. *Quart. J. Roy. Meteor. Soc.*, **122**, 1963–1967, doi:10.1002/qj.49712253611.
- Davis, C., 2015: The formation of moist vortices and tropical cyclones in idealized simulations. *J. Atmos. Sci.*, **72**, 3499–3516, doi:10.1175/JAS-D-15-0027.1.
- Dee, D., and Coauthors, 2011: The ERA-Interim reanalysis: Configuration and performance of the data assimilation system. *Quart. J. Roy. Meteor. Soc.*, **137**, 553–597, doi:10.1002/qj.828.
- Delanoë, J., and R. J. Hogan, 2010: Combined *CloudSat*–*CALIPSO*–*MODIS* retrievals of the properties of ice clouds. *J. Geophys. Res.*, **115**, D00H29, doi:10.1029/2009JD012346.
- , —, R. M. Forbes, A. Bodas-Salcedo, and T. H. M. Stein, 2011: Evaluation of ice cloud representation in the ECMWF and UK Met Office models using *CloudSat* and *CALIPSO* data. *Quart. J. Roy. Meteor. Soc.*, **137**, 2064–2078, doi:10.1002/qj.882.
- Emanuel, K., A. A. Wing, and E. M. Vincent, 2014: Radiative-convective instability. *J. Adv. Model. Earth Syst.*, **6**, 75–90, doi:10.1002/2013MS000270.
- Hartmann, D. L., and K. Larson, 2002: An important constraint on tropical cloud-climate feedback. *Geophys. Res. Lett.*, **29**, 1951, doi:10.1029/2002GL015835.
- Holloway, C. E., and S. J. Woolnough, 2016: The sensitivity of convective aggregation to diabatic processes in idealized radiative-convective equilibrium simulations. *J. Adv. Model. Earth Syst.*, **8**, 166–195, doi:10.1002/2015MS000511.
- Huffman, G. J., and Coauthors, 2007: The TRMM Multisatellite Precipitation Analysis (TMPA): Quasi-global, multiyear, combined-sensor precipitation estimates at fine scales. *J. Hydrometeorol.*, **8**, 38–55, doi:10.1175/JHM560.1.

- Igel, M. R., A. J. Drager, and S. C. van den Heever, 2014: A CloudSat cloud object partitioning technique and assessment and integration of deep convective anvil sensitivities to sea surface temperature. *J. Geophys. Res. Atmos.*, **119**, 10 515–10 535, doi:10.1002/2014JD021717.
- Janowiak, J. E., R. J. Joyce, and Y. Yarosh, 2001: A real-time global half-hourly pixel-resolution infrared dataset and its applications. *Bull. Amer. Meteor. Soc.*, **82**, 205–217, doi:10.1175/1520-0477(2001)082<0205:ARTGHH>2.3.CO;2.
- Jeevanjee, N., and D. M. Romps, 2013: Convective self-aggregation, cold pools, and domain size. *Geophys. Res. Lett.*, **40**, 994–998, doi:10.1002/grl.50204.
- Johnson, R. H., T. M. Rickenbach, S. A. Rutledge, P. E. Ciesielski, and W. H. Schubert, 1999: Trimodal characteristics of tropical convection. *J. Climate*, **12**, 2397–2418, doi:10.1175/1520-0442(1999)012<2397:TCOTC>2.0.CO;2.
- Khairoutdinov, M., and K. Emanuel, 2010: Aggregated convection and the regulation of climate. *29th Conf. on Hurricanes and Tropical Meteorology*, Tucson, AZ, Amer. Meteor. Soc., P2.69. [Available online at https://ams.confex.com/ams/29Hurricanes/techprogram/paper_168418.htm.]
- Langhans, W., K. Yeo, and D. M. Romps, 2015: Lagrangian investigation of the precipitation efficiency of convective clouds. *J. Atmos. Sci.*, **72**, 1045–1062, doi:10.1175/JAS-D-14-0159.1.
- Liu, C., and E. J. Zipser, 2009: “Warm rain” in the tropics: Seasonal and regional distributions based on 9 yr of TRMM data. *J. Climate*, **22**, 767–779, doi:10.1175/2008JCLI2641.1.
- Liu, Z., R. Marchand, and T. Ackerman, 2010: A comparison of observations in the tropical western Pacific from ground-based and satellite millimeter-wavelength cloud radars. *J. Geophys. Res.*, **115**, D24206, doi:10.1029/2009JD013575.
- Marchand, R., G. G. Mace, T. Ackerman, and G. Stephens, 2008: Hydrometeor detection using CloudSat—An Earth-orbiting 94-GHz cloud radar. *J. Atmos. Oceanic Technol.*, **25**, 519–533, doi:10.1175/2007JTECHA1006.1.
- , J. Haynes, G. G. Mace, T. Ackerman, and G. Stephens, 2009: A comparison of simulated cloud radar output from the multiscale modeling framework global climate model with CloudSat cloud radar observations. *J. Geophys. Res.*, **114**, D00A20, doi:10.1029/2008JD009790.
- Mauritsen, T., and B. Stevens, 2015: Missing iris effect as a possible cause of muted hydrological change and high climate sensitivity in models. *Nat. Geosci.*, **8**, 346–351, doi:10.1038/ngeo2414.
- Muller, C., and I. M. Held, 2012: Detailed investigation of the self-aggregation of convection in cloud-resolving simulations. *J. Atmos. Sci.*, **69**, 2551–2565, doi:10.1175/JAS-D-11-0257.1.
- , and S. Bony, 2015: What favors convective aggregation and why? *Geophys. Res. Lett.*, **42**, 5626–5634, doi:10.1002/2015GL064260.
- Nair, A. K. M., K. Rajeev, M. K. Mishra, B. V. Thampi, and K. Parameswaran, 2012: Multiyear lidar observations of the descending nature of tropical cirrus clouds. *J. Geophys. Res.*, **117**, D18201, doi:10.1029/2011JD017406.
- Pendergrass, A., and D. Hartmann, 2014: Changes in the distribution of rain frequency and intensity in response to global warming. *J. Climate*, **27**, 8372–8383, doi:10.1175/JCLI-D-14-00183.1.
- Qu, X., A. Hall, S. A. Klein, and A. M. DeAngelis, 2015: Positive tropical marine low-cloud cover feedback inferred from cloud-controlling factors. *Geophys. Res. Lett.*, **42**, 7767–7775, doi:10.1002/2015GL065627.
- Reed, K. A., B. Medeiros, J. T. Bacmeister, and P. H. Lauritzen, 2015: Global radiative–convective equilibrium in the Community Atmosphere Model, version 5. *J. Atmos. Sci.*, **72**, 2183–2197, doi:10.1175/JAS-D-14-0268.1.
- Stein, T. H. M., J. Delanoë, and R. J. Hogan, 2011a: A comparison among four different retrieval methods for ice-cloud properties using data from CloudSat, CALIPSO, and MODIS. *J. Appl. Meteor. Climatol.*, **50**, 1952–1969, doi:10.1175/2011JAMC2646.1.
- , D. J. Parker, J. Delanoë, N. S. Dixon, R. J. Hogan, P. Knippertz, R. I. Maudiment, and J. H. Marsham, 2011b: The vertical cloud structure of the West African monsoon: A 4 year climatology using CloudSat and CALIPSO. *J. Geophys. Res.*, **116**, D22205, doi:10.1029/2011JD016029.
- Stephens, G. L., and Coauthors, 2002: The CloudSat mission and the A-Train. *Bull. Amer. Meteor. Soc.*, **83**, 1771–1790, doi:10.1175/BAMS-83-12-1771.
- , S. van den Heever, and L. A. Pakula, 2008: Radiative–convective feedbacks in idealized states of radiative–convective equilibrium. *J. Atmos. Sci.*, **65**, 3899–3916, doi:10.1175/2008JAS2524.1.
- Sui, C.-H., X. Li, and M.-J. Yang, 2007: On the definition of precipitation efficiency. *J. Atmos. Sci.*, **64**, 4506–4513, doi:10.1175/2007JAS2332.1.
- Tan, J., C. Jakob, W. Rossow, and G. Tselioudis, 2015: Increases in tropical rainfall driven by changes in frequency of organized deep convection. *Nature*, **519**, 451–454, doi:10.1038/nature14339.
- Tobin, I., S. Bony, and R. Roca, 2012: Observational evidence for relationships between the degree of aggregation of deep convection, water vapor, surface fluxes, and radiation. *J. Climate*, **25**, 6885–6904, doi:10.1175/JCLI-D-11-00258.1.
- , —, C. E. Holloway, J.-Y. Grandpeix, G. Sèze, D. Coppin, S. J. Woolnough, and R. Roca, 2013: Does convective aggregation need to be represented in cumulus parameterizations? *J. Adv. Model. Earth Syst.*, **5**, 692–703, doi:10.1002/jame.20047.
- Tompkins, A. M., and G. C. Craig, 1998: Radiative–convective equilibrium in a three-dimensional cloud-ensemble model. *Quart. J. Roy. Meteor. Soc.*, **124**, 2073–2097, doi:10.1002/qj.49712455013.
- Trenberth, K., A. Dai, R. Rasmussen, and D. Parsons, 2003: The changing character of precipitation. *Bull. Amer. Meteor. Soc.*, **84**, 1205–1217, doi:10.1175/BAMS-84-9-1205.
- van de Poll, H. M., H. Grubb, and I. Astin, 2006: Sampling uncertainty properties of cloud fraction estimates from random transect observations. *J. Geophys. Res.*, **111**, D22218, doi:10.1029/2006JD007189.
- Virts, K. S., and J. M. Wallace, 2010: Annual, interannual, and intraseasonal variability of tropical tropopause transition layer cirrus. *J. Atmos. Sci.*, **67**, 3097–3112, doi:10.1175/2010JAS3413.1.
- Wing, A. A., and K. A. Emanuel, 2014: Physical mechanisms controlling self-aggregation of convection in idealized numerical modeling simulations. *J. Adv. Model. Earth Syst.*, **6**, 59–74, doi:10.1002/2013MS000269.
- , and T. W. Cronin, 2016: Self-aggregation of convection in long channel geometry. *Quart. J. Roy. Meteor. Soc.*, **142**, 1–15, doi:10.1002/qj.2628.
- , S. Camargo, and A. H. Sobel, 2016: Role of radiative–convective feedbacks in spontaneous tropical cyclogenesis in idealized numerical simulations. *J. Atmos. Sci.*, **73**, 2633–2642, doi:10.1175/JAS-D-15-0380.1.
- Wood, R., and C. S. Bretherton, 2006: On the relationship between stratiform low cloud cover and lower-tropospheric stability. *J. Climate*, **19**, 6425–6432, doi:10.1175/JCLI3988.1.
- Zelinka, M. D., and D. L. Hartmann, 2010: Why is longwave cloud feedback positive? *J. Geophys. Res.*, **115**, D16117, doi:10.1029/2010JD013817.
- Zhang, D., Z. Wang, and D. Liu, 2010: A global view of midlevel liquid-layer topped stratiform cloud distribution and phase partition from CALIPSO and CloudSat measurements. *J. Geophys. Res.*, **115**, D00H13, doi:10.1029/2009JD012143.